

Resonant capacitive MEMS acoustic emission transducers

(*Smart Materials and Structures*, accepted for publication)

Resonant capacitive MEMS acoustic emission transducers

D Ozevin^{1,5}, D W Greve², I J Oppenheim³, and S P Pessiki⁴

¹Physical Acoustics Corporation, Princeton Junction, NJ 08550; Email: dozevin@pacndt.com

²Department of Electrical and Computer Engineering, Carnegie Mellon University, Pittsburgh, PA 15213; Email: dg07@andrew.cmu.edu

³Department of Civil and Environmental Engineering, Carnegie Mellon University, Pittsburgh, PA 15213; Email: ijo@cmu.edu

⁴Department of Civil and Environmental Engineering, Lehigh University, Bethlehem, PA 18015; Email: spp1@lehigh.edu

⁵Formerly Department of Civil and Environmental Engineering, Lehigh University, Bethlehem, PA 18015

Abstract. We describe resonant capacitive MEMS transducers developed for use as acoustic emission detectors, fabricated in the commercial three-layer polysilicon surface micromachining process (MUMPs). The 1-cm square device contains six independent transducers in the frequency range between 100 kHz and 500 kHz, and a seventh transducer at 1 MHz. Each transducer is a parallel plate capacitor with one plate free to vibrate, thereby causing a capacitance change which creates an output signal in the form of a current under DC bias voltage. With the geometric proportions we employed, each transducer responds with two distinct resonant frequencies. In our design the etch hole spacing was chosen to limit squeeze film damping and thereby produce an underdamped vibration when operated at atmospheric pressure. Characterization experiments obtained by capacitance and admittance measurements are presented, and transducer responses to physically simulated AE source are discussed. Finally, we report our use of the device to detect acoustic emissions associated with crack initiation and growth in weld metal.

Keywords. Acoustic emissions, capacitance, MEMS, resonance, sensor, ultrasonics.

1. Introduction

Sensors for structural health monitoring should provide for easy installation and sensitive detection of structural degradation. Acoustic emission testing or monitoring is often used for this purpose, and is particularly attractive because it detects stress waves released as structural damage occurs. Acoustic emissions are transient stress waves generated by rapid release of energy from localized sources within a material such as crack initiation and growth, and are characterized as bursts of ultrasonic energy, mostly at frequencies between about 100 kHz and 1 MHz [1]. Transducers used for acoustic emission detection have included non-contact optical sensing [2], fiber optic sensing [3], and capacitive sensing [4]. However, the most practical transducers for routine structural health monitoring are piezoceramic (PZT) transducers, either resonant or broad-band. PZT acoustic emission transducers are similar to PZT accelerometers except that the proof mass is replaced by a backing material to control damping [5]. The characteristics of the damping material and other geometric parameters determine the transducer bandwidth. Broadband piezoelectric transducers respond to emissions over the entire range of relevant frequencies, although generally with lower sensitivity than resonant types. Resonant transducers have higher sensitivity but detect only a portion of the frequency range of interest.

While piezoceramic transducers are well established in this application, they are relatively expensive and therefore not ideal for permanent installation. This work is directed at the development and characterization of MEMS-based transducers for acoustic emission. MEMS transducers can be small and inexpensive in large scale production, and can incorporate additional electronics either on the same chip or in a second chip integrated in the same package. A further advantage of a MEMS device is the ability to include several transducers with different resonant frequencies on the chip. Each transducer can have a relatively narrow resonant frequency (and thus high sensitivity) while still providing information from the entire frequency range of interest. This additional information should provide improved understanding of the damage processes, and should help discriminate between mechanical noise and true acoustic emission events.

In prior work on MEMS transducers for acoustic emission, Schoess and Zook [6] used a cantilever with an optical detection scheme, whereas Varadan and Varadan [7] noted the possibility of detecting acoustic emission with a comb-type transducer. A MEMS transducer more closely related to our work was reported by Jones et al. [8], and its response to pencil lead break excitation was studied.

In this paper, we consider a device containing an array of MEMS transducers with different resonant frequencies. We first describe the transducer mechanics, and then describe the design of the acoustic emission transducer array. We report electrical characterization testing, verification of device operation, and its response to acoustic emission events physically simulated by pencil lead breaks. We conclude with a discussion of results obtained in structural testing, including a side-by-side comparison with a conventional piezoceramic transducer.

2. Transducer mechanics

Figure 1 depicts the mechanical and electrical elements of the acoustic emission transducer in schematic form. The transducer contains one electrode fixed to the package and thereby to the substrate, and a second electrode, a diaphragm, that is free to vibrate; in the at-rest position the electrodes are separated by gap g . The diaphragm is modeled as mass m , attached to the package by springs with total stiffness k . The two electrodes form a parallel plate capacitor, and under a DC voltage bias, termed V_{DC} , the vibration of the diaphragm produces a time-varying current. Based on our observations in laboratory testing [9], transducer sensitivity is determined largely by the mechanical Q of the diaphragm spring-mass system, and is most significantly influenced by squeeze-film damping caused by the movement of air in the gap between the fixed electrode and the diaphragm.

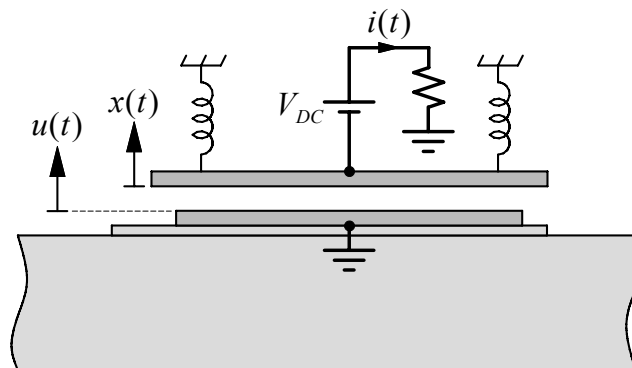


Figure 1. Schematic of acoustic emission transducer showing both mechanical and electrical elements.

Resonant capacitive MEMS acoustic emission transducers

We consider excitation of the transducer by a time-dependent substrate displacement $u(t)$, and denote the position of the diaphragm with respect to the fixed electrode as $g+x(t)$. The equation of motion for $x(t)$ takes the familiar form of a spring-mass system subjected to base excitation $u(t)$:

$$m\ddot{x} + c\dot{x} + kx = -m\ddot{u} \quad (1)$$

where m is the mass in kg, k is the spring constant in N/m, and c is a viscous damping constant in N-s/m. The resonant frequency of the system is ω_0 , rad/s, defined as

$$\omega_0 = \sqrt{\frac{k}{m}} \quad (2)$$

and the quality factor Q is defined as

$$Q = \frac{m\omega_0}{c}. \quad (3)$$

The device is a parallel plate capacitor with area A , undergoing a time-varying change in its gap dimension. In the presence of constant bias voltage V_{DC} , the output signal is a current $i(t)$ that varies with the velocity of the diaphragm relative to the fixed electrode. Expanding about the at-rest gap dimension g , the output signal is:

$$i(t) = V_{DC} \frac{dC}{dt} = V_{DC} \frac{\epsilon_0 A}{g^2} \dot{x} \quad (4)$$

The Laplace transform of output signal expressed in terms of excitation $u(t)$ is

$$I(s) = V_{DC} \frac{\epsilon_0 A}{g^2} \frac{-s^3}{s^2 + \omega_0^2 + s\omega_0/Q} U(s) \quad (5)$$

where $I(s)$ and $U(s)$ are the Laplace transforms of the (output) current $i(t)$ and excitation $u(t)$, respectively.

Based upon known characteristics of acoustic emission events and upon our past experimental studies, we envision the event to possess some sustained energy content around the resonant frequency of the sensor. The cases subsequently analyzed in this paper involve the steady-state response to sinusoidal excitation of amplitude u_m when driven at resonance, for which the amplitude of the output signal is

$$i_m = V_{DC} \frac{\epsilon_0 A}{g^2} \omega_0 Q u_m \quad (6)$$

The highest sensitivity at a given resonant frequency results from maximizing Q . However, very high values of the Q would produce long ringing which could cause the transducer to miss closely spaced excitations. In our opinion, a modestly underdamped condition is desirable, and accordingly our target design values for Q were in the range of 5 to 15, allowing for reasonably short decay times while permitting the entire frequency range of interest to be spanned with a small number of transducers.

3. Transducer Design

The transducer design should achieve moderate underdamped Q and span resonant frequencies in the range from 100 kHz to 1 MHz. The gap should be as small as attainable in the process used, and the total sensor area should be large enough to provide a reasonable output current magnitude. In this section we outline the design of suitable transducers, and in subsequent sections we report the results of electrical characterization, and the response of the transducers to acoustic emissions.

In our design each diaphragm unit is square in plan, with side L_u , and is supported by 16 L-shaped springs, which are arrayed in four pinwheels anchored at the symmetrical quarter-points, each pinwheel being formed by four L-shaped springs. The distal and proximal segments of each spring have lengths denoted L_{s1} and L_{s2} , respectively, as shown in figure 2. Transducers, modeled as spring-mass systems, were designed at six different translational frequencies between 100 and 500 kHz; the mass was changed by varying L_u , the stiffness was changed by varying L_{s2} , and the diaphragm was modeled as a rigid mass. In each transducer, N diaphragm units are packed into a square area and act in parallel to achieve target capacitances between 30 and 40 pF. (A seventh transducer was designed for a resonant frequency near 1 MHz and is not addressed in this paper.)

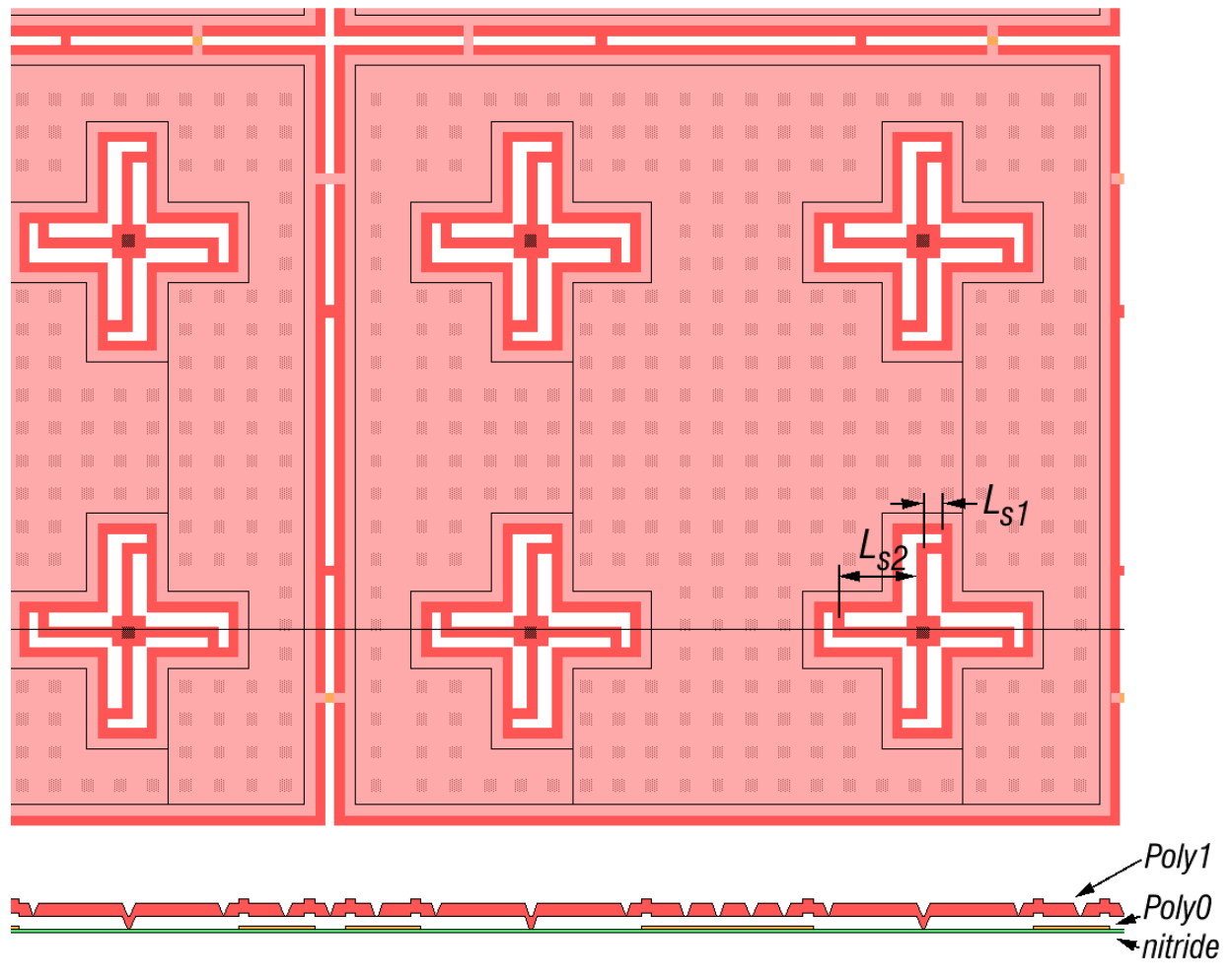


Figure 2. CAD layout and section views of one diaphragm unit, with connections to neighboring units.

Resonant capacitive MEMS acoustic emission transducers

The effective spring constant per diaphragm unit, designated as k_u , results from a combination of elastic bending and torsion in both segments of the L-shaped springs. Assuming the diaphragm and anchor to be rigid, k_u is calculated [9] as

$$k_u = \frac{16}{\left[\frac{L_{s1}^3}{3EI} + \frac{L_{s1}^2 L_{s2}}{GJ} + \frac{L_{s2}^3}{3EI} \right] - \left[\frac{L_{s1}^2}{2EI} + \frac{L_{s1} L_{s2}}{GJ} \right] \left[\frac{L_{s1}}{EI} + \frac{L_{s2}}{GJ} \right] \left[\frac{L_{s1}^2}{2EI} + \frac{L_{s1} L_{s2}}{GJ} \right]} \quad (7)$$

where

$$I = \frac{b_s h_s^3}{12} \quad (8)$$

and

$$J = \beta b_s h_s^3 \quad (9)$$

E is the elastic modulus, 160 GPa, and G is the shear modulus, 65.0 GPa, of polysilicon. The width and thickness of each spring is b_s , 4 μm , and h_s , 2 μm , respectively; those dimensions are used to calculate the moment of inertia, I , and are combined with the torsion coefficient β (0.229 for this particular rectangular cross-section) to yield the St. Venant torsional constant J . The mass density of the polysilicon is 2300 kg/m^3 , which is used when calculating the mass a diaphragm unit, m_u .

Transducers were designed in the poly-MUMPS surface micromachined process [10] which has three layers of polysilicon. The transducers were designed using the POLY0 layer to form the fixed electrode and the POLY1 layer to form the suspended diaphragm. The gap between the two polysilicon layers in the MUMPS process is nominally 2 μm , but can be reduced by a nominal 0.75 μm through use of a DIMPLE mask level, which was employed here. Table 1 lists the most important transducer dimensions, and figure 3 shows the CAD layout.

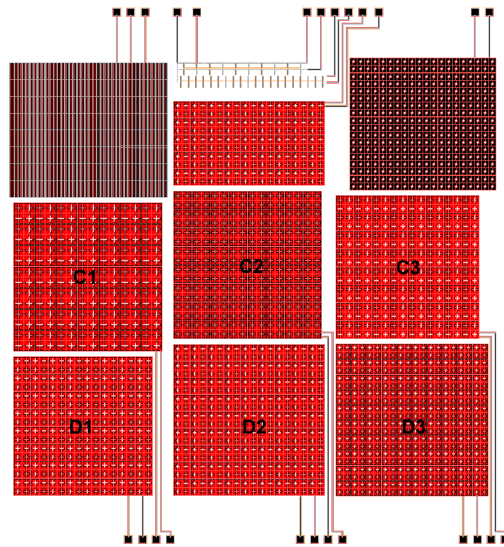


Figure 3. CAD layout of the sensor chip.

Table 1. Transducer dimensions.

Transducer	N	L _{s1} μm	L _{s2} μm	L _u μm
C1	49	8	45	380
C2	64	8	40	330
C3	64	8	33	320
D1	64	8	27	310
D2	81	8	22	300
D3	100	8	19	270

4. Transducer characterization

The completed and released MEMS chips were mounted in a 64-pin ceramic package, wirebonded, and characterized electrically by capacitance measurements and by impedance measurements. Capacitance measurements, as a function of DC bias taken at 1 MHz, were used to extract the approximate value of the gap g and to verify the calculated value of the spring constants k_u . Remote from resonance, capacitance as a function of DC bias V_{DC} is determined [9] as follows

$$C(V_{DC}) = C_0 + C_0^2 \frac{V_{DC}^2}{2Ng^2k_u} = C_0 + C_1V_{DC}^2 \quad (10)$$

where N is the number of diaphragms comprising the transducer, k_u is the spring constant per diaphragm unit, C_0 is the capacitance at rest which depends on gap g , and C_1 is a constant expressing the increase in capacitance with the squared value of the DC bias voltage which depends upon k_u .

The capacitance C_0 is composed of contributions from area on the periphery, A_p , where POLY1 overlaps POLY0 with no DIMPLE, and a larger area on the interior, A_i , where POLY1 overlaps POLY0 with DIMPLE. The total area occupied by a diaphragm unit is A , which is greater than A_p and A_i combined because of the area occupied by springs, etch release holes, and spaces between diaphragms. Defining g as the gap dimension on the interior, the capacitance is

$$C_0 = \frac{\epsilon_0 A_i}{g} + \frac{\epsilon_0 A_p}{(g + 0.75 \mu m)} \quad (11)$$

where the dimension of 0.75 μm reflects the greater plate separation in regions on the periphery. The values of C_0 and C_1 were determined by fitting the measured characteristics of $C(V_{DC})$, and are presented in Table 2; the areas listed in Table 2 were extracted directly from the CAD files, and do not reflect the nominal dimensions referred to elsewhere. The C_0 values for all six transducers were consistent with a gap $g = 1.05 \mu m$, somewhat smaller than the nominal gap of 1.25 μm in the DIMPLE region [9]. Values of C_1 were calculated based on the calculated spring constant k_u and upon the gap dimension of 1.05 μm determined from the C_0 measurements. The calculated values of C_1 are in acceptable agreement with, but consistently higher than, the measured values.

Table 2. Transducer capacitance and area parameters.

Transducer	A_p μm^2	A_i μm^2	A μm^2	$C_{0(\text{calc})}$ pF	$C_{0(\text{meas})}$ pF	k_u N/m	$C_{1(\text{calc})}$ fF/V ²	$C_{1(\text{meas})}$ fF/V ²
C1	14016	91111	118759	41.0	40	224	69	45
C2	12448	62728	87240	37.8	39	320	32	23
C3	11136	62006	83894	37.0	36	560	17	11
D1	7712	58012	78812	33.7	34	1024	7.9	6
D2	7232	54917	74117	40.4	40	1856	4.9	3
D3	6560	42663	60135	39.2	40	2832	2.5	2

Measured values of C_1 are consistently smaller than predicted, which may result from approximations in calculation of the spring constant, the elastic flexibility of the diaphragm, or variations in manufacturing. In order to study the first two possibilities we performed finite element simulations using the static linear mode of the structural mechanics module of FEMLAB. Figure 4 shows the deformed shape of the D1 diaphragm under a DC bias of 5 V, which is a reasonable approximation to the lowest mode shape in translation. The simulations show that there is considerable elastic distortion of the plate, with the maximum deflection approximately 33% greater than the average deflection. With that average plate deflection, C_1 is recalculated to be 6.9 fF/V², between the values of 7.9 and 6 fF/V² obtained from the lumped mass calculations and from the measurements, respectively. This suggests that at least some of the disagreement is due to the assumption of a rigid diaphragm made in the lumped mass calculations.

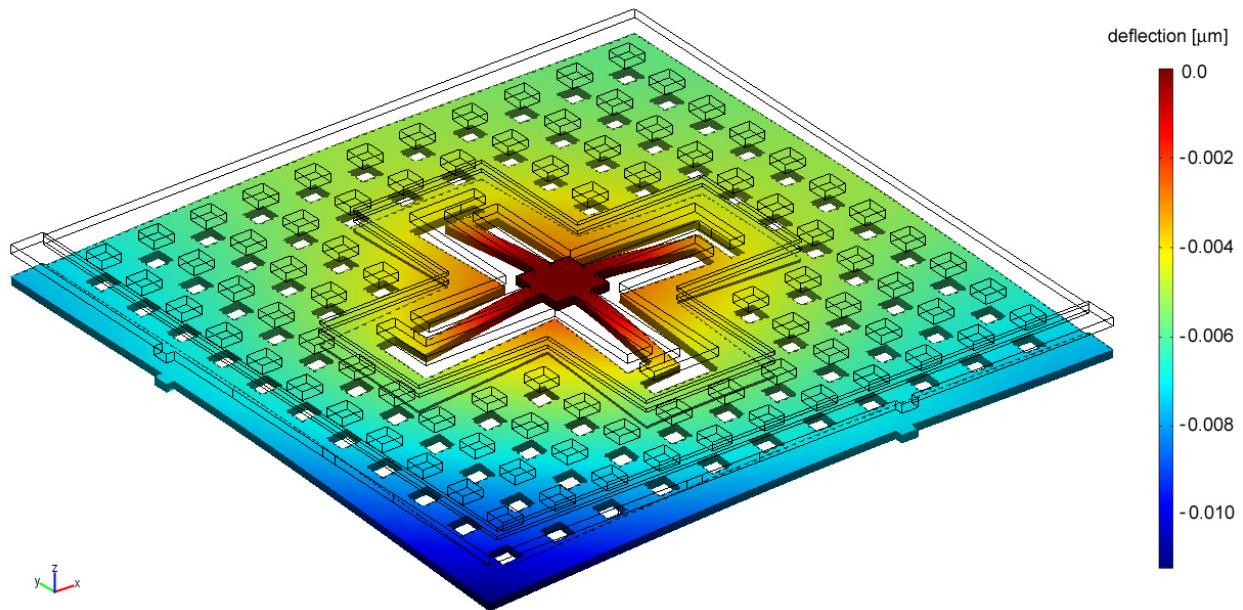


Figure 4. One-quarter of a D1 diaphragm, deflected by a 5 V bias

As a lumped mass system, one resonance was expected in translation and two were expected in rocking, but only the translational mode should be active electrically. Table 3 lists the diaphragm mass m_u and spring constant k_u for each transducer, the predicted (lumped mass) resonant frequency in translation, and the two lowest resonant frequencies obtained from swept-frequency admittance measurements under an applied DC bias. We attribute the presence of two electrically active resonances to the combination of the spring-mass system translational mode with the lowest symmetrical bending mode of the diaphragm.

Table 3. Transducer resonant frequencies.

Transducer	m_u kg	k_u N/m	$f_{(\text{calc})}$ kHz	f_1 kHz	f_2 kHz
C1	5.53E-10	224	101	107	150
C2	4.07E-10	320	141	150	207
C3	3.91E-10	560	191	178	252
D1	3.67E-10	1024	266	187	275
D2	3.45E-10	1856	369	210	317
D3	2.8E-10	2832	506	272	405

We now consider the dynamic characteristics of the transducers. The measured admittance for a lumped-mass system resonant at the frequency ω_0 is [11]

$$Y = j\omega C_0 + \frac{V_{DC}^2 C_0^2}{mg^2} \frac{j\omega}{\omega_0^2 - \omega^2 + j\omega\omega_0/Q} \quad (12)$$

The Q factor is defined in (3) and is inversely proportional to the viscous damping constant c . We now observe that c contains three contributions

$$c = c_{poly} + c_{holes} + c_{emission} \quad (13)$$

where c_{poly} is due to internal losses in the polysilicon, which are known from past experimental studies to be small in comparison to the two other loss mechanisms; c_{holes} is due to squeeze-film damping from air flow into and out of the etch holes, and $c_{emission}$ is due to dissipation by emission (radiation) into the air.

In our previous experience with similar structures [11], etch holes were spaced near the maximum allowed by design rules, which resulted in an overdamped condition at atmospheric pressure and required those transducers to be operated in vacuum. In this design the spacing of etch holes was reduced. A simplified model for the damping constant is obtained by assuming a piston within a circular cylinder of radius b_o , containing a central vent (etch) hole of radius b_i ; an area-conserving constraint is applied to convert the square etch holes and grid in the real structure to b_o and b_i in the simplified model. The pressure, $p(r)$, developed against the piston as the air is forced through the etch hole is obtained as [11]

$$p(r) = \left\{ \left[\frac{r^2}{4} - \frac{b_i^2}{4} + (\ln b_i - \ln r) \frac{b_o^2}{2} \right] \frac{12\mu}{g^3} \right\} \dot{x} \quad (14)$$

The force acting against the face of the piston is then expressed by a dashpot constant

$$c_{onehole} = 2\pi \int_{b_i}^{b_o} \left\{ \right\} r dr \quad (15)$$

The damping constant c_{holes} is then approximated as (15) multiplied by the number of etch holes in the diaphragm. The etch holes are 5 μm square on a 13 μm grid, converting into 2.82 μm and 7.33 μm , respectively, for b_i and b_o .

The dissipation from emission (radiation) into air is given [11] by

$$c_{emission} = Z_{air} A \quad (16)$$

where $Z_{air} = 430 \text{ kg/m}^2\text{-s}$ is the acoustic impedance of air and A is the area of a diaphragm unit.

The second and third terms in (13) are absent in vacuum; losses in the polysilicon are small, and a relatively high Q is observed [11]. Figure 5 shows the measured admittance under vacuum for transducer C2 (black dashed line), and two sharp resonances are observed, as noted earlier. Figure 5 also shows the admittance magnitude as a function of frequency for C2 and for two other transducers at atmospheric pressure. In all cases, two resonances are prominent under vacuum conditions (not shown for transducers D2 and D3) and close examination of the measurements shows that both broadened resonances remain visible at atmospheric pressure. Also shown in the figure are fits to the data using two modes.

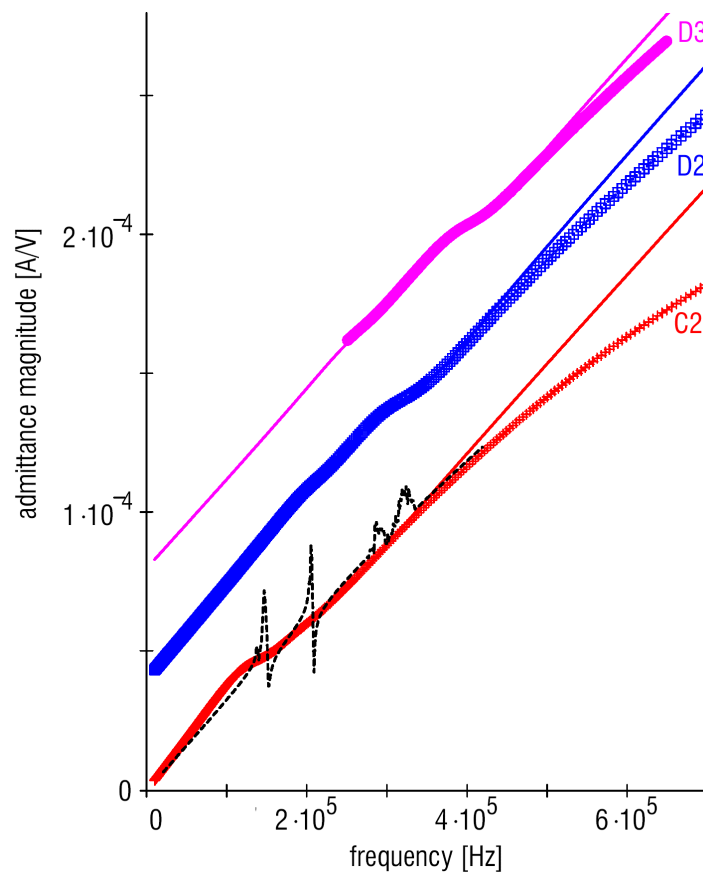


Figure 5. Admittance magnitude as a function of frequency for three transducers: (black) C2 transducer with $V_{DC} = 5 \text{ V}$, vacuum; (red, crosses) C2 with $V_{DC} = 5 \text{ V}$, atmospheric pressure; (blue, squares) D2 at $V_{DC} = 10 \text{ V}$, atmospheric pressure, and (magenta, circles) D3 at $V_{DC} = 10 \text{ V}$, atmospheric pressure. Fits to the data are shown as solid lines.

Results obtained from fits to data, at atmospheric pressure, are presented in Table 4. Table 4 also lists the Q factors, calculated from (12), for that frequency. The agreement is very good at low frequencies and fair at higher frequencies.

Table 4. Comparison of measured and predicted frequencies and Q factors.

Transducer	$f_{(\text{calc})}$ kHz	$f_{1(\text{meas})}$ kHz	$f_{2(\text{meas})}$ kHz	$Q_{1(\text{meas})}$	$Q_{1(\text{calc})}$
C1	101	107	150	1.3	1.3
C2	141	150	207	1.3	1.8
C3	191	178	252	1.6	2.5
D1	266	187	275	1.7	3.1
D2	369	210	317	2.5	4.3
D3	506	272	405	3.1	5.7

5. Transducer response to excitation

We report here testing of the transducers using acoustic emission signals physically simulated by pencil lead breaks [9]. Initial characterization was performed using pencil lead breaks directly on the ceramic package in order to avoid complications of acoustic coupling through interfaces. We will also briefly report comparison between the MEMS acoustic emission transducer and conventional transducers in a realistic environment.

Figure 6 shows the measurement circuit for an acoustic emission transducer, where C_{p1} and C_{p2} represent parasitic capacitances to substrate ground and R_{in} represents the input impedance of a preamplifier. In this work, the preamplifier is an operational amplifier circuit with a gain of 10. In this circuit, C_{p1} and C_{p2} are the parasitic capacitances from the POLY0 and POLY1 electrodes to the substrate, plus any additional wiring capacitance. The capacitance C_{p2} is minimized by using nearly the minimum size allowed by the design rules for the POLY1 supports. Referring to figure 3, C_{p2} is about 10% of C_0 for the transducers in row D, and about 20% of C_0 for the transducers in row C. Provided $R_{in} > 1/j\omega C_0$, essentially all the current i flows through C_0 , and consequently the output voltage under harmonic excitation is

$$V_{out}(t) = \frac{V_{DC}}{g} \frac{C_0}{C_0 + C_{p2}} \frac{Q}{j} e^{j\omega t} \quad (17)$$

The results of functional testing of the transducers are shown in figure 7. The DC bias was 9 V, and a pencil lead break on the ceramic package was used to simulate an acoustic emission signal. Signals with magnitude of approximately 50 mV were observed for all transducers. It is important to note that a previous transducer design [9] showed detectable response to pencil lead breaks only when operated under vacuum. The fast Fourier transform of the observed signals shows that transducers with higher resonant frequencies exhibit somewhat greater response at higher frequencies.

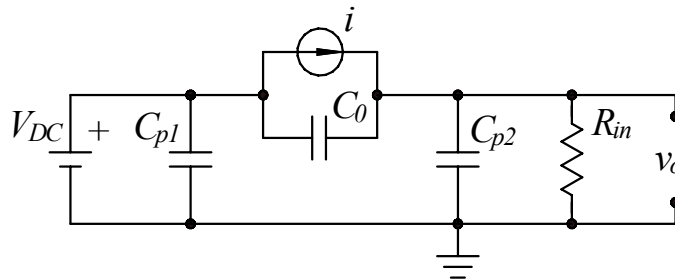


Figure 6. Measurement circuit for tests of the acoustic emission transducer.

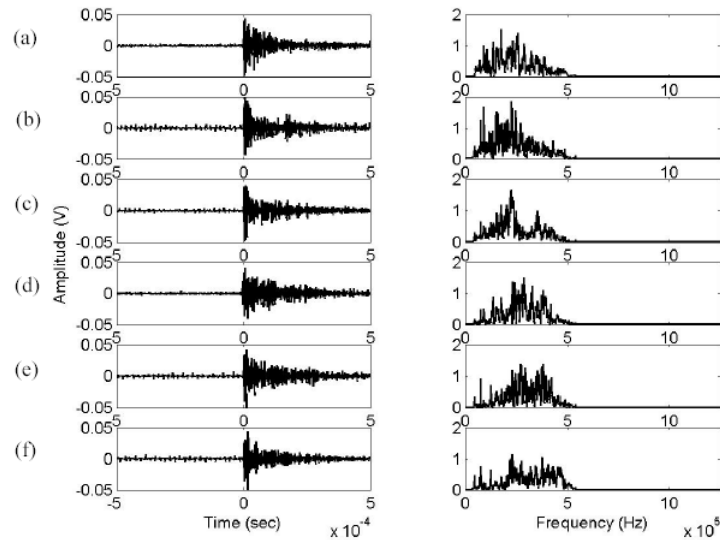


Figure 7. Response of the MEMS acoustic emission transducer to a pencil lead break on the ceramic package. (Shown, top to bottom: C1, C2, C3, D1, D2, and D3 transducers)

6. Transducer application to structural testing

The MEMS transducers were applied in a series of laboratory structural tests, in which their performance was compared on a side-by-side basis with that of a conventional piezoceramic transducer (Physical Acoustics Corporation model R30, with a resonant frequency of approximately 300 kHz).

The specimen used was prepared from two GR50 steel plates measuring approximately 41.4 cm long, 2.5 cm thick and 30.5 cm wide that were welded along their 10° beveled cut ends to create a plate with a length of 82.8 cm. The plates were welded using E70T-4 electrodes. The welded steel plate assembly was then saw cut into five pieces. After the surfaces of each beam specimen were machined to have smooth and flat surfaces, a straight through notch was machined into the weld metal in each beam specimen. The notch included a 60° angle and 0.25 mm root radius. The four beam specimens were then subjected to a 35.6 kN maximum repeated load at a frequency of 10 Hz for about 15000 cycles using a three-point bending set-up. This created a fatigue precrack with a depth of about 3 mm from the root of the notch. Preliminary experiments were performed with three specimens in order to test the data acquisition system. Results are reported for an experiment on a single specimen.

As shown in figure 8, the MEMS device and the conventional acoustic emission transducer were attached to the precracked steel beam specimen loaded in 4-point bending, over a span of 76 cm, in an Instron 4400R testing machine. The conventional and MEMS acoustic emission transducers were located 3.8 cm and 8.9 cm away from the crack, respectively and were coupled to the specimen with vacuum grease (PAC R30) or cyanoacrylate adhesive (MEMS). Signals from five different MEMS transducers, biased with a DC voltage of 9 V, were collected along with the signal from the conventional transducer. All signals were amplified with a gain of 20; the circuit employed for the MEMS sensor had a bandwidth of approximately 2 MHz, and the amplifier used for the conventional sensor was a Ithaco 1201 preamplifier operated at its bandpass setting (-3 dB bandwidth at least 400 kHz). The signals were digitized by a National Instruments 5112 DAQ board (MEMS D2 and D3 at 2 MS/s, for a sample duration of 50 ms) and a Tektronix TDS2014 oscilloscope (MEMS C1, C2, C3 and PAC R30 at 1 MS/s, for a sample duration of 2.5 ms), and Labview programs were used to control the testing machine and data acquisition. Trigger signals for the oscilloscope and DAQ board were obtained from the PAC R30 transducer; after each trigger event, records were written to hard disk under computer control. The testing machine load

Resonant capacitive MEMS acoustic emission transducers

and displacement were also recorded as a function of time for correlation with the acoustic emission records.

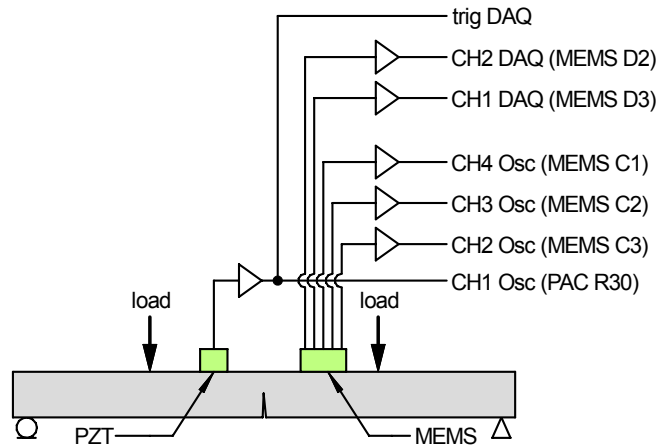


Figure 8. Experimental arrangement for transducer testing.

We describe results for one complete experiment in which a test specimen was loaded into the failure range. The crosshead displacement was increased linearly at a rate of 0.025 mm/min, and figure 9 shows the load-displacement plot. Acoustic emission events detected by the piezoelectric transducer are indicated as red circles. The behavior is initially linearly elastic and no acoustic emission events are observed; the slight stiffening visible at the beginning of the load-displacement plot results from compression of polypropylene bearing pads used at the support and load points. At a load of about 20 kN, acoustic emission events begin to be observed and the load-displacement plot becomes distinctly nonlinear. A large load drop occurs at about 23.5 kN, associated with a substantial crack propagation. After this load drop, acoustic emission events continue to be observed until a second load drop, at which point the experiment was terminated. The test specimen showed significant permanent deformation after unloading.

In figure 9, an appreciable number of acoustic emission events are observed prior to the first load drop. Detection of these events is the objective of acoustic emission testing, as these events indicate that the member is sustaining damage and crack growth. In the following, we will compare the acoustic emission events detected by the conventional piezoelectric and MEMS transducers.

Resonant capacitive MEMS acoustic emission transducers

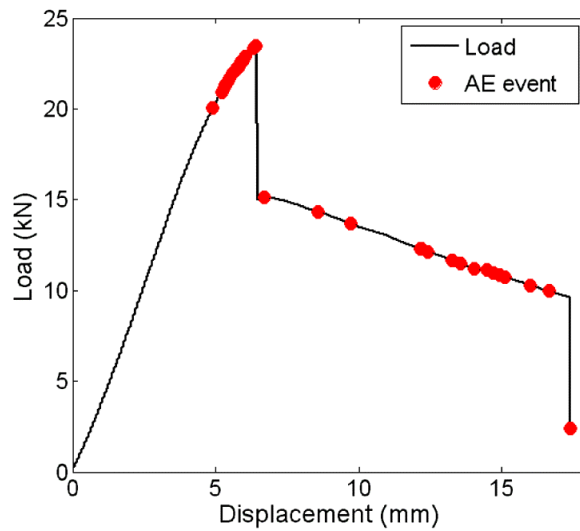


Figure 9. Load-displacement characteristic with acoustic emission events detected by the conventional transducer indicated as red circles.

Figure 10 compares the signal from the C2 MEMS transducer and the piezoceramic transducer for an acoustic emission event at a load of 21.3 kN. Both transducers unambiguously detect the acoustic emission event, although the piezoelectric transducer has a larger signal level and better signal to noise ratio. The signal to noise ratio for the two signals in Fig. 10 is about 16 dB for the MEMS transducer (150 kHz) and better than 46 dB for the piezoelectric transducer (300 kHz). The sensitivity of transducers can be compared [12] using the value of the transformer ratio n , defined as the ratio between the output current and the wave velocity normal to the surface. This transformer ratio is generally greater for piezoelectric transducers than for MEMS capacitive transducers, unless very small values of the gap g are used. The higher noise level, which can be reduced with better shielding, is due in part to electrical interference in the chassis and housing used in the laboratory tests.

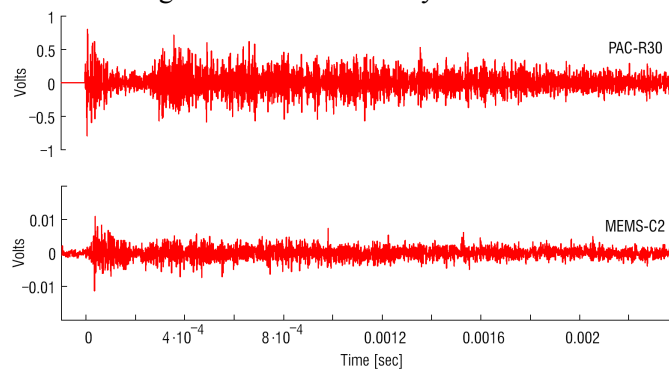


Figure 10. Comparison of signals detected by the piezoelectric transducer (top trace) and the MEMS transducer (bottom trace) at 21.3 kN.

Because of the lower signal-to-noise ratio, not all acoustic emission events detected with the piezoelectric transducer were detected by the MEMS transducer. In this experiment, a total of 33 events were detected by the piezoelectric transducer. The MEMS device detected 9 of the 17 events prior to the first load drop at 23.5 kN. This experiment shows that the present MEMS transducer design is sufficiently sensitive to detect acoustic events indicative of damage and crack growth. The MEMS transducer signal levels are

Resonant capacitive MEMS acoustic emission transducers

lower than that of the commercial piezoceramic device, although this is of less concern than the signal-to-noise ratio, and therefore improvement of the SNR is desirable.

MEMS transducers offer the possibility of simultaneous detection by multiple redundant transducers, as well as event detection by transducers with different resonant frequencies. Such multiple-mode sensing may assist in discriminating between real and spurious signals, and Figure 11 shows the simultaneous detection by five different MEMS transducers of an acoustic emission event at a load of 21.1 kN. However, the laboratory tests were found to be free of spurious (nonstructural) events, and therefore the utility of multiple-mode sensing has not been tested.

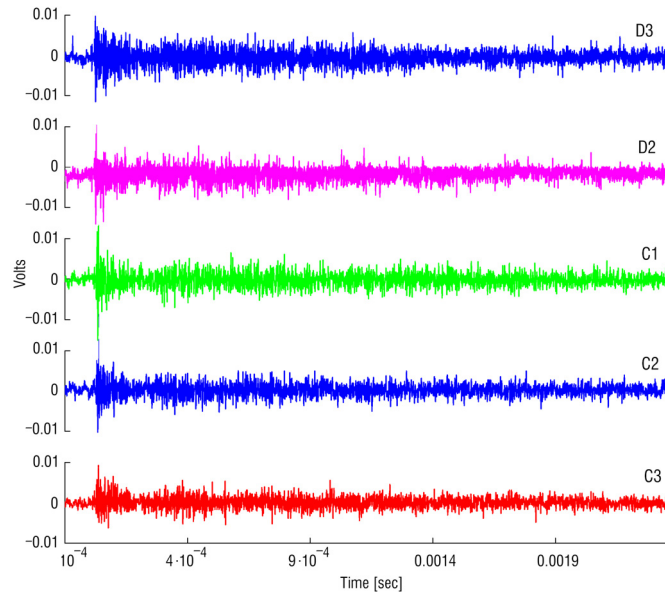


Figure 11. Simultaneous detection of an acoustic emission event by five MEMS transducers.

7. Summary

We have shown that a MEMS chip containing multiple resonant, capacitive-type vibration transducers is a practical device for detecting acoustic emission signals. The resonant frequency of each transducer is determined by the spring constant and the effective mass of the supported diaphragm. A moderately underdamped behavior is desired, which has been achieved by appropriate choice of the etch hole spacing. We have demonstrated the detection of acoustic emission events associated with damage, in a structural member undergoing crack initiation and growth. In a side-by-side comparison with a commercial piezoceramic transducer, fewer acoustic emission events were detected by the MEMS transducer. This was a consequence of the somewhat worse signal-to-noise ratio of the MEMS transducer, in part as a result of electrical interference. However, we believe that the signal-to-noise ratio can be improved with better packaging and shielding.

Acknowledgements

The authors thank N. Tyson for conducting the admittance measurements, and an anonymous reviewer for suggesting improvements to the submitted manuscript. We also thank the Pennsylvania Infrastructure Technology Alliance and the National Science Foundation for support. This material is based upon work supported by the National Science Foundation under Grant No. CMS-0329880. Any opinions, findings, and conclusions or recommendations expressed in this material are those of the authors and do not necessarily reflect the views of the National Science Foundation.

- [1] Stephens R W and Pollock A A 1971 Waveforms and Frequency Spectra of Acoustic Emission *J. Acoust. Soc. Amer.* **50** 904-910
- [2] Kline R A, Green R E and Palmer C H 1978 A Comparison of Optically and Piezoelectrically Sensed Acoustic Emission Signals *J. Acoust. Soc. Amer.* **64** 1633-1639
- [3] Yang Y C and Han K S 2002 Damage Monitoring and Impact Detection using Optical Fiber Vibration Sensor *Smart Materials and Structures* **11** 337-345
- [4] Breckenridge F R and Greenspan M 1981 Surface-wave Displacement: Absolute Measurements using a Capacitive Transducer *J. Acoust. Soc. Amer.* **69** 1177-1185
- [5] Gautschi G 2001 *Piezoelectric Sensorics* (Berlin: Springer-Verlag)
- [6] Schoess J N and Zook J D 1998 Test results of a resonant integrated microbeam sensor (RIMS) for acoustic emission monitoring *Proc. SPIE* **3328** 326-32
- [7] Varadan V K and Varadan V V 1999 Microsensors and MEMS for health monitoring of composite and aircraft structures in flight *Proc. SPIE* **3673** 359-68
- [8] Jones A R D, Noble R A, Bozeat R J and Hutchins D A 1999 Micromachined Ultrasonic Transducers for Damage Detection in CFRP Composites *Proc. SPIE* **3673** 369-78
- [9] Ozevin D I 2005 Capacitive MEMS Transducers for Acoustic Emission Testing of Materials and Structures (Bethlehem, PA: Lehigh University Ph.D. Dissertation)
- [10] Koester D A, Mahadevan R, Hardy B and Markus K W 2001 *MUMPS Design Handbook Revision 7.0* (Research Triangle Park, NC: Cronos)
- [11] Oppenheim I J, Jain A and Greve D W 2003 Electrical Characterization of Coupled and Uncoupled MEMS Ultrasonic Transducers *IEEE Trans. Ultrasonics, Ferroelectrics, Frequency Control* **50** 297-304
- [12] Oppenheim I J, Jain A and Greve D W 2003 MEMS Ultrasonic Transducers for the Testing of Solids *IEEE Trans. Ultrasonics, Ferroelectrics, Frequency Control* **50** 305-311